LAWRENCE
LIVERMORE
NATIONAL
LABORATORY

LLNL-JRNL-641758

Thermodynamic interpretation of reactive processes in Ni-Al nanolayers from atomistic simulations

L. Sandoval, G. H. Campbell, J. Marian

August 1, 2013

Modeling and Simulation in Materials Science and Engineering

Disclaimer

Thermodynamic interpretation of reactive processes in Ni-Al nanolayers from atomistic simulations

Luis Sandoval ‡, Geoffrey H. Campbell, Jaime Marian
Lawrence Livermore National Laboratory

Abstract. Metals which can form intermetallic compounds by an exothermic reaction constitute a class of reactive materials with multiple applications. Ni-Al laminates of thin alternating layers are being considered as model nanometric metallic multilayers for studying various reaction processes. However, the reaction kinetics at short timescales after mixing are not entirely understood. In this work, we calculate the free energies of Ni-Al alloys as a function of composition and temperature for different solid phases using thermodynamic integration based on state-of-the-art interatomic potentials. We use this information to interpret molecular dynamics (MD) simulations of bilayer systems at 800 and 1000 K, and find that an amorphous phase forms upon mixing as a precursor to a more stable nano crystalline B2 phase. Simulated times of up to 30 ns were achieved, which provides a window to phenomena not previously observed in MD. Our simulations provide insight into the early experimental reaction timescales and suggest that changes in local composition govern the thermodynamic evolution of Ni-Al laminates.

‡ Currently at Theoretical Division T-1, Los Alamos National Laboratory, Los Alamos, NM 87545, USA.

1. Introduction

Solid reactive materials that form intermetallic compounds via high energy release are increasingly being used in multiple materials science processes [1–3]. These systems have the advantage that both reactants and products are confined to the condensed state, which makes them helpful in anaerobic conditions and where gaseous products are non-desirable. For these reasons, there is a wide range of applications where they are now being used, such as welding, propellants, heat initiators, etc. Ni-Al systems are an important subclass of reactive materials due to the formation of intermetallic phases with high temperature strength and high resistance to oxidation [4, 5].

Because of their many attractive properties and promising applications, Ni-Al reactive systems have attracted significant attention over the last two decades, both experimental [6–9] and theoretical [10, 11]. The formation of Ni-Al intermetallics is an intrinsically atomistic process, governed by the free energies of the different phases involved as well as the kinetics of atomic and interfacial motion. With the advent of efficient simulation codes and reliable interatomic potentials, molecular dynamics (MD) has emerged as an ideal tool to investigate these reactive processes. However, despite the number of MD studies performed to date [12–15], a comprehensive thermodynamic picture of the reaction processes is still lacking. In this paper, we use state-of-the-art interatomic potentials to calculate the free energies of different Ni-Al phases. We then use this thermodynamic information to interpret and understand the reactive behavior of Ni-Al nano layers. We carry out simulations at 800 and 1000 K, which are known to be above the temperature of self ignition in NiAl (≈600 K). We find that a recrystallized B2 phase forms from a local amorphous phase caused primarily by the penetration of Ni into the Al layer.

This paper is organized as follows. In Section 2, we describe the simulation method in detail, as well as the thermodynamic integration technique employed. We then begin Section 3 providing the cold equation of state for several solid phases of equiatomic Ni-Al, followed by the free energy results as a function of alloy composition, and a description of Ni-Al bicrystal reaction kinetics. We finalize in Section 4 with a discussion of our findings and the conclusions.

2. Methods

All calculations presented here were carried out with the `lammps` code [16] using 256 processors on Livermore Computing's parallel architectures. We employ the embedded-atom method (EAM) interatomic potential for Ni-Al developed by Purja and Mishin [17]. This potential is particularly suitable for simulations of heterophase interfaces and mechanical behavior of Ni-Al alloys. Additionally, the melting points of fcc Ni and Al are well reproduced by the potential, which adds confidence to the high temperature calculations that will be presented here. Except where noted, we consider periodic systems at zero total pressure.

To compute free energies we use thermodynamic integration using Kirkwood's coupling parameter method [18–21], also known as λ-*integration*. In the canonical ensemble, the free energy difference, $\Delta F = F_B - F_A$, between two systems A and B characterized by potential energy functions U_A and U_B can be obtained by integrating along a reversible path from A to B. The distance along this path can be measured by using a potential energy function that uses a switching parameter λ:

$$U(\lambda) = (1-\lambda)U_A + \lambda U_B \tag{1}$$

The canonical partition function for such a system can be written as:

$$Q(N;\Omega;T;\lambda) = \frac{1}{\Lambda^{3N}N!}\int d\boldsymbol{r}^N \exp\left\{-\beta U(\lambda)\right\} \tag{2}$$

where N is the number of particles, Ω is the system volume, T is the absolute temperature, and $\beta = (k_B T)^{-1}$ is the reciprocal temperature with k_B being Boltzmann's constant. From eq. 2 the Helmholtz free energy can be calculated as $F = -k_B T \ln Q$, whose derivative with respect to the switching parameter can be written as:

$$\left.\frac{\partial F(\lambda)}{\partial \lambda}\right|_{N,\Omega,T} = -\frac{1}{\beta}\frac{\partial}{\partial\lambda}\ln Q = -\frac{1}{\beta Q}\frac{\partial Q}{\partial \lambda} = \frac{\int d\boldsymbol{r}^N \frac{\partial U(\lambda)}{\partial\lambda}\exp\left\{-\beta U(\lambda)\right\}}{\int d\boldsymbol{r}^N \exp\left\{-\beta U(\lambda)\right\}} \tag{3}$$

which is the expression of an ensemble average that can be calculated via molecular dynamics simulations. From this, the free energy difference between systems A and B is given by:

$$\Delta F = F(U_A) - F(U_B) = \int_0^1 \left\langle \frac{\partial U}{\partial\lambda}\right\rangle d\lambda = \int_0^1 \langle U_B - U_A\rangle\, d\lambda \tag{4}$$

Although amorphous structures are also of interest in this work, a system of Einstein oscillators is appropriate as a reference state (characterized by U_B) as long as internal diffusive processes (thermodynamic aging) are negligible on the scale of the simulations:

$$U_B(\boldsymbol{r}) = \frac{\alpha}{2}\sum_{i=1}^{N}\left(\boldsymbol{r}_i - \boldsymbol{r}_{0,i}\right)^2 \tag{5}$$

where α is a spring constant§ and $\{\boldsymbol{r}_0\}$ are the equilibrium positions. After accounting for the use of periodic boundary conditions and fixing the center of mass in MD simulations, the free energy of a system of harmonic oscillators can be obtained analytically as:

$$F(U_B) = -\frac{3NkT}{2}\left\{\log\frac{m\alpha^{N-1}}{h^2(kT)^{N-2}} + \frac{1}{3N}\log\frac{N}{\Omega^2}\right\} \tag{6}$$

where m and h are the atomic mass and Planck's constant.

The free energy of the system at temperatures other than the reference temperature used in the above process can be found by recourse to the Gibbs-Helmholtz integral:

$$\frac{F_1}{T_1} = \frac{F_0}{T_0} + \int_{T_0}^{T_1}\frac{E(n,\Omega,T)}{\tau^2}d\tau \tag{7}$$

where E is the internal energy, which can be computed as:

$$E(T) = \langle U(T)\rangle \tag{8}$$

By way of example, Figure 1 shows the calculation of the integrand in eq. 4 as a function of λ for several alloy compositions in random bcc and amorphous Ni-Al phases at 500 K. The curves represent cubic polynomial fits to the data points. Integration of these curves as in eq. 4 yields the free energy of the system. Sufficient sampling is critical, particularly when $\langle\partial U/\partial\lambda\rangle$ changes quickly, to ensure an accurate calculation of the free energy integral.

§ For numerical reasons, it is best to choose α in eq. 5 such that:

$$\alpha = \frac{kT}{\langle\Delta r^2\rangle}$$

where Δr^2 is the mean square displacement of the target phase.

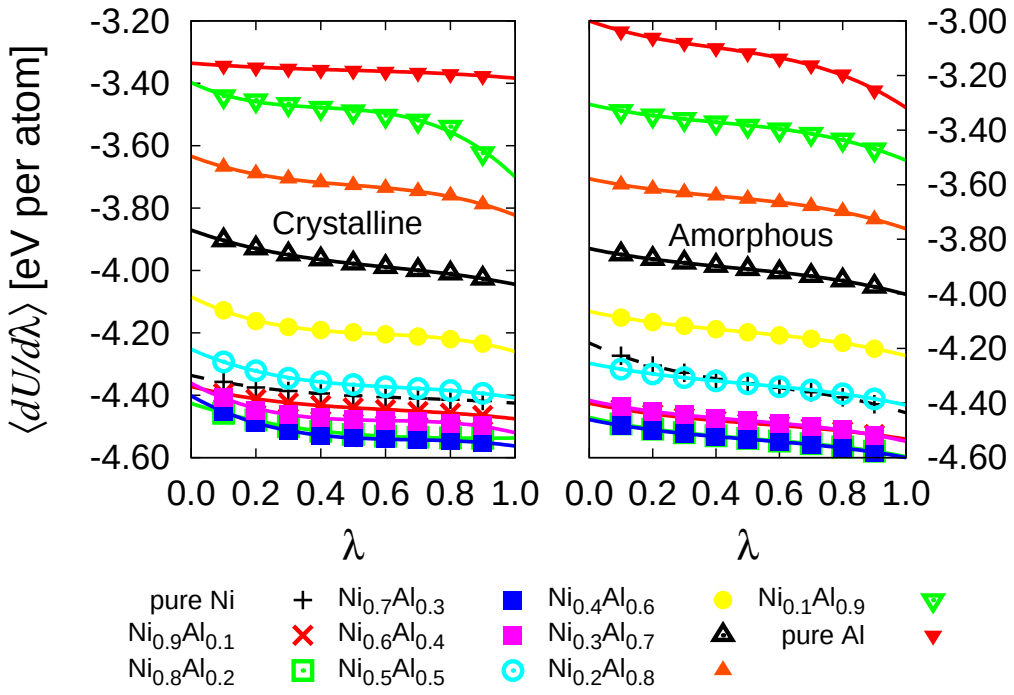

Figure 1: Calculation of the integrand in eq. 4 as a function of λ for several alloy compositions in random bcc (crystalline) and amorphous Ni-Al phases at 500 K. The curves represent cubic polynomial fits to the data points. Integration of these curves as in eq. 4 yields the free energy of the system. In the crystalline case, the pure Ni and Al phases correspond to fcc crystals, as opposed to a bcc (B2) phase for a given atomic composition. Note that the vertical scale is different in both graphs.

3. Results

3.1. Equiatomic NiAl

First we present results for equiatomic systems (Ni_1Al_1) containing 16,000 atoms. We study four distinct phases, namely, the ordered fcc $L1_0$, ordered (B2) and disordered (random solid solution) bcc phases, and an amorphous phase obtained from quenching a liquid system (equilibrated for 100 ps at 3000 K) at a cooling rate

Table 1: Equilibrium volumes, densities, and lattice parameters at 0 K for the four equiatomic Ni-Al phases considered here (from Fig. 2). The lattice parameter has been obtained assuming bcc lattice cells for the B2 and random phases and an fcc lattice for the $L1_0$ structure. The amorphous phase does not have an associated underlying lattice structure and hence no equilibrium lattice parameter has been calculated. The last two columns show the values of the thermal expansion coefficient and heat capacity at 800 K, obtained from Figs. 3 and 4.

Solid phase	Ω_0 [Å^3]	ρ_0 [$\times 10^{28}$ m^{-3}]	a_0 [Å]	α_t [$\times 10^{-5}$ K^{-1}]	C_p [eV atom^{-1} K^{-1}]
B2	11.4	8.81	2.83	4.53	2.8×10^{-4}
$L1_0$	11.9	8.40	3.62	4.15	2.8×10^{-4}
Amorphous	12.4	8.06	–	6.05	2.6×10^{-4}
Random bcc	12.1	8.26	2.89	2.73	2.1×10^{-4}
fcc Ni	10.9	9.17	3.52	2.76	2.7×10^{-4}
fcc Al	16.9	5.91	4.05	5.24	2.7×10^{-4}

of 300 K ps^{-1} [22].

3.1.1. Equilibrium volume and thermal expansion. The thermal expansion coefficient $\alpha_t(T)$ is obtained from the temperature dependence of the atomic volume Ω_a:

$$\alpha_t = \frac{1}{\Omega_0}\frac{d\Omega_a}{dT} \tag{9}$$

where Ω_0 is a reference atomic volume (usually taken as the value at 0 K). We first compute Ω_0 for the four phases indicated above from energy-volume relations. The evolution of the cohesive energy as a function of atomic volume (and density) is shown in Figure 2 for each phase. From the figure, one can obtain the equilibrium values as those corresponding to a minimum of the cohesive energy (indicated by vertical dashed lines in Fig. 2). The numerical values in each case are given in Table 1. The figure also gives the relative stability of each phase at zero temperature, with the B2 phase always being the most stable.

Next we calculate the variation of the atomic volume with temperature using simulations in the isothermal-isobaric ensemble (NpT). Results for all four phases considered here are shown in Fig. 3. For the B2 and $L1_0$ systems, α_t monotonically

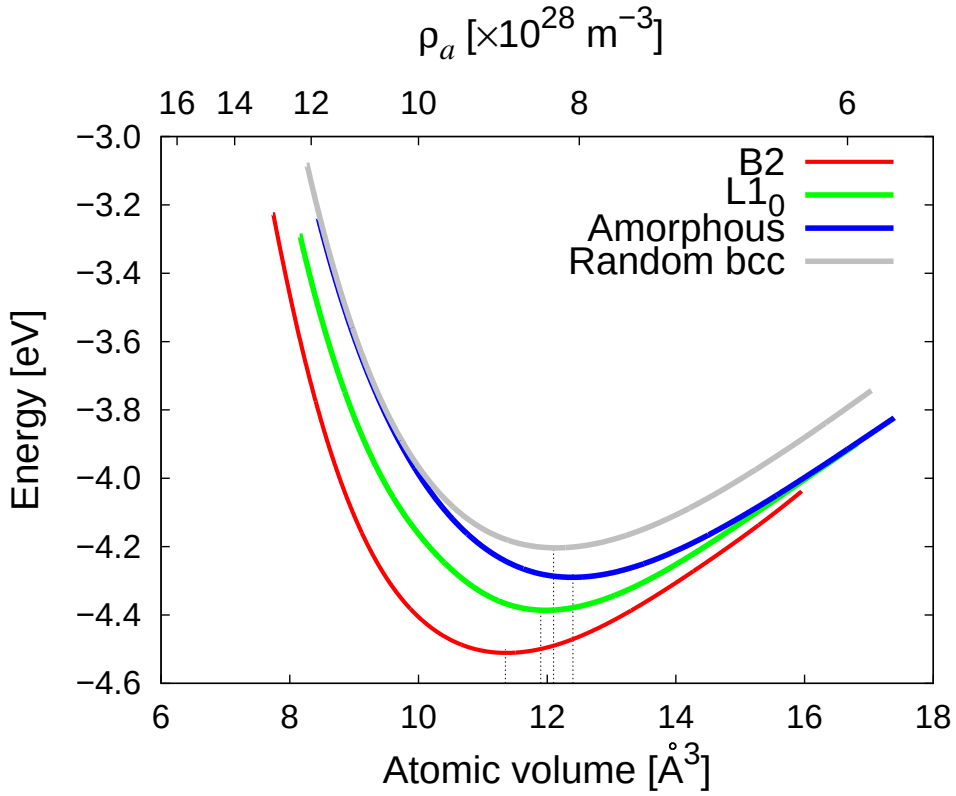

Figure 2: Cohesive energy of four different equiatomic Ni-Al phases as a function of atomic volume Ω_a (or, equivalently, atomic density ρ_a). The vertical dashed lines indicate the location of the minimum for each curve, given in Table 1.

increases, while for the amorphous phase, the thermal expansion coefficient suffers a marked increase as the melting point is approached. The random bcc phase displays an upward trend with some roughness associated with it, probably a consequence of increased internal diffusion processes as temperature is elevated. The values of α_t at 800 K in each case are given in Table 1.

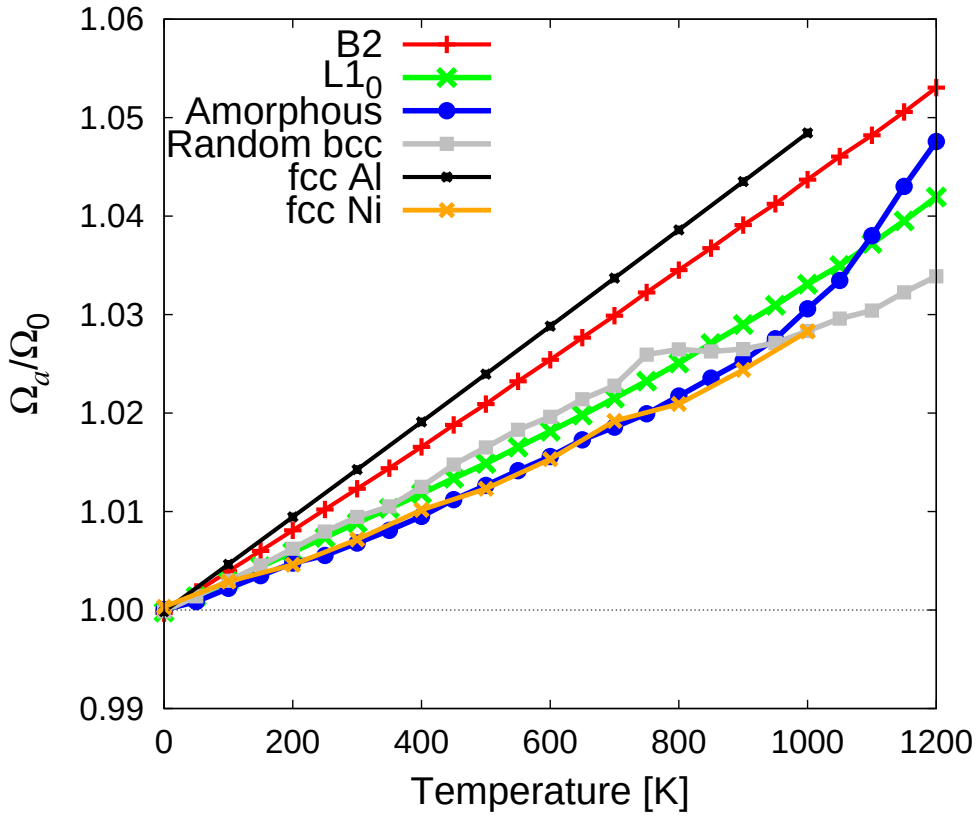

Figure 3: Variation of the atomic volume with temperature for the four different equiatomic Ni-Al phases considered here. The reference atomic volumes Ω_0 are those given in Table 1 for each case.

3.1.2. Free energies. From equation 8, we compute the internal energies as a function of temperature for all the different equiatomic phases as well as for pure fcc Ni and Al for comparison. Results are shown in Figure 4, with all systems exhibiting linear dependencies except the amorphous one at temperatures approaching 1200 K. From these data, the heat capacity at zero pressure can be

calculated straightforwardly as

$$C_p = \left(\frac{\partial H}{\partial T}\right)_P = \left(\frac{\partial E}{\partial T}\right)_P$$

because at zero pressure $H \equiv E$. The results at 800 K for each phase are given in Table 1. These calculations are a precursor to obtaining the free energies as a function of temperature (cf. eq. 7), which are given in Figure 5. Figure 5 establishes the relative stability of each phase as a function of temperature. The B2 phase is the most stable of all the phases considered here over the entire temperature range, while the amorphous state displays the highest free energy among the NiAl compounds. However, at 800 K and above the relative stability of the amorphous, $L1_0$, and random bcc phases with respect to one another is only marginal. This has important implications for the reaction kinetics of Ni-Al bilayers that will be studied below.

3.2. Free energies of Ni_xAl_y alloys

During the early stages of reactive mixing, the system will probe a wide spectrum of compositions corresponding to different Ni/Al atomic ratios (Ni_xAl_y). Locally, the x:y ratio can be far from unity, depending on fluctuations set by the temperature and the relative diffusivity of each species. This means that the kinetic evolution of the reaction front is set by fluctuations, *i.e.* variations in local composition, temperature, etc. Thus, it is also of interest to calculate the free energy as a function of composition c (which represents the Ni concentration) for selected phases. Since mixing processes involve high entropy and therefore low order, here we focus on the amorphous and random bcc phases as potential precursors of thermodynamically stable (ordered) Ni_xAl_y alloys. Figure 6 shows the free energy surface $F(c,T)$ for the two phases of interest. Derivatives of $F(c,T)$ with respect each one of the axes give the entropy (temperature axis) and the chemical potential (concentration axis). The information contained in Fig. 6 can be used to define the phase diagram between these two structures, although neither of these phases are equilibrium phases and thus are typically not considered in Ni-Al phase diagrams.

As the free energy surface shows, the free energy differences between the random bcc and amorphous phases is small, with the crystalline phase generally being more stable than the amorphous one, except roughly for $0.1 < c < 0.2$, and, interestingly, at $c \approx 0.9$ and $T > 600$ K. Additionally, the free energies are minimum for Ni

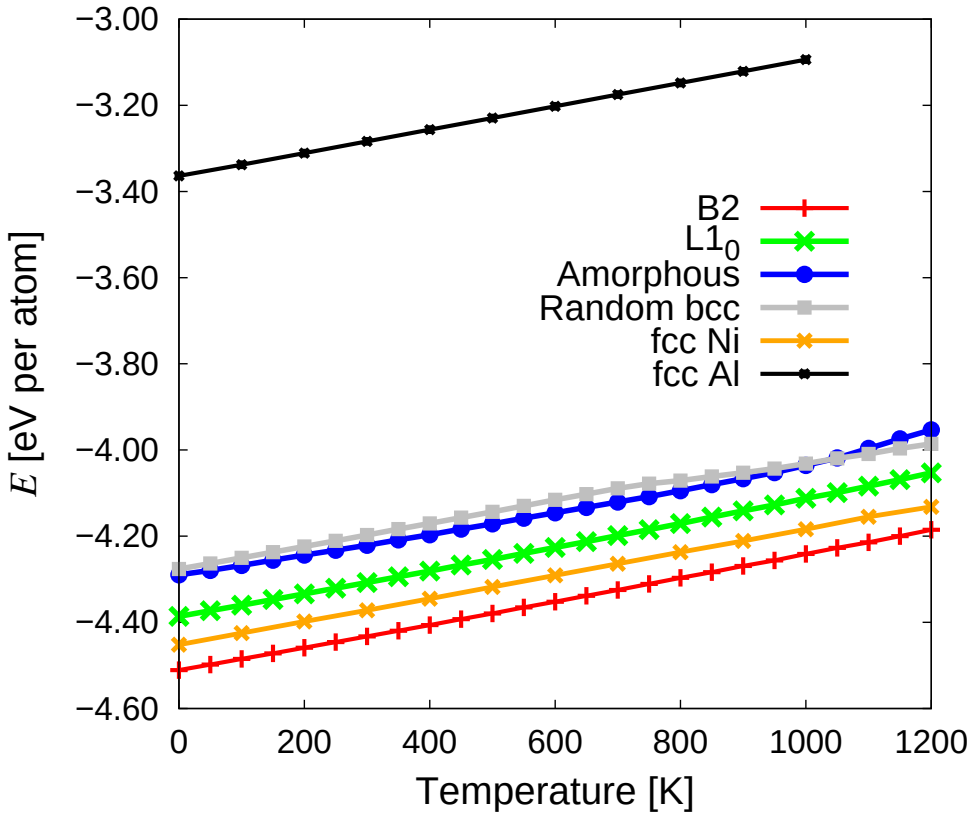

Figure 4: Internal energies as a function of temperature of the four equiatomic Ni-Al phases considered. The internal energies of pure Ni and Al are also shown for reference.

concentrations around $c = 0.8$. We believe this to be an indirect indicator of the stability of the Ni_3Al system.

3.3. Reaction kinetics

We now study the reactivity of a Ni-Al bilayer at 800 K. The simulated system consists of two crystallites of Ni and Al containing, respectively, $N = 313,600$ and 329,251 atoms. The Ni and Al subsystems are fcc lattices oriented in the same

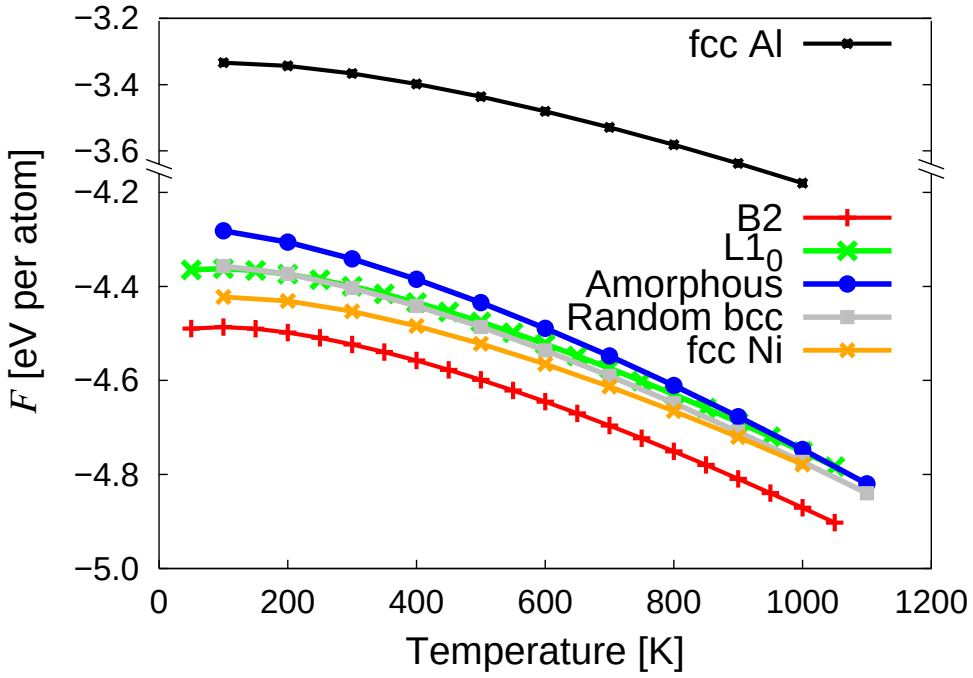

Figure 5: Free energies as a function of temperature of the four equiatomic Ni-Al phases considered. The free energies of pure Ni and Al are also shown for reference.

direction and separated by an interface with a surface normal oriented along the [100] direction. Periodic boundary conditions are used along each coordinate. Crone *et al* have shown that the ignition temperature (at which a self-sustaining reaction is achieved) depends on the misfit interface strain [23]. To avoid such dependency, we use the columnar arrangement employed by Baras and Politano [24] which ensures a strain-free interface after relaxation. The initial dimensions of the Ni and Al layers are, respectively, 19.6×8.8×19.6 nm, and 17.5×17.5×17.5 nm. This provides for an empty 1-nm thick buffer on which the Al subsystem can expand relaxing all interfacial

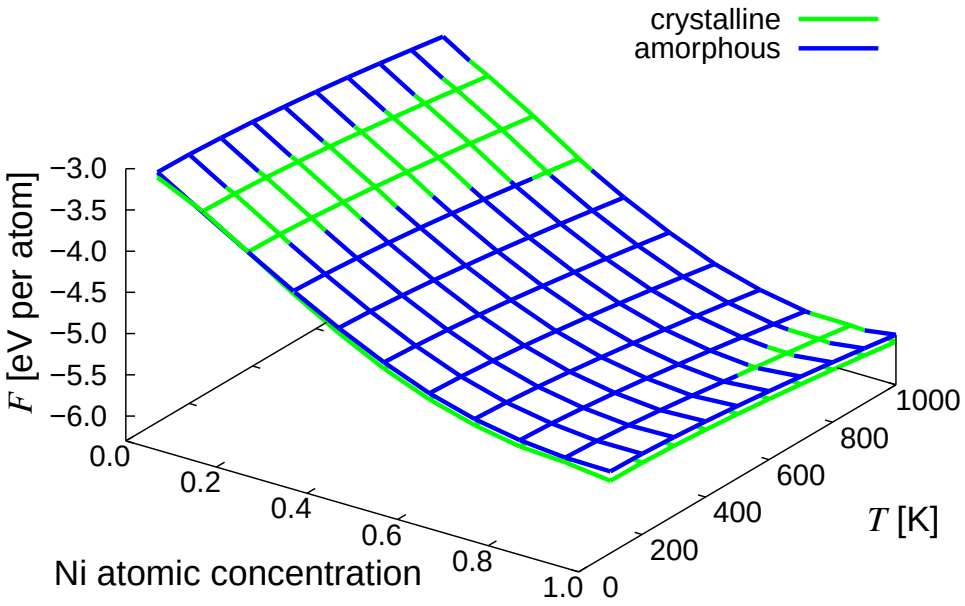

Figure 6: Free energies of amorphous and disordered bcc phases as a function of temperature and atomic composition. The crystalline phase corresponds to a random B2 (bcc) phase except for the pure Ni and Al phases (c=1.0 and 0.0), which have fcc structure.

stresses.

The bicrystal is initially equilibrated at the target temperature of 800 K by means of an inverse simulated annealing. This is done by heating the system from 0 K at a rate of 1 K ps^{-1} so that it takes 0.8 ns to reach the desired temperature of 800 K. The simulations are all run in the NpT ensemble to ensure that there are no internal stresses that might affect the reaction process. This annealing procedure results in some diffusive mixing prior to reaching 800 K. Therefore, on the Al side of the original interface at $t = 0$, the initial state corresponds to an Al-rich phase with some interpenetrated Ni. This Al-rich phase retains its original fcc order but

we have confirmed that it does not correspond to an ordered $L1_0$ structure. On the Ni side of the original interface, the penetration of Al is quite limited, resulting in essentially a very dilute fcc Ni-Al phase. This picture is consistent with relative interdiffusion coefficients that are 3.3 times larger for Ni in Al than the reverse [25]. A sequence of snapshots from the 30-ns reaction simulation is given in Figure 7. The initial stages of the reaction process, now at a constant temperature of 800 K, are a continuation of the main features of the annealing (sample preparation) process, namely, swift penetration of Ni atoms in the fcc Al crystal and limited Al diffusion in Ni. Eventually this leads to the formation of an amorphous phase in the Al-rich region, as confirmed by pair correlation function $g(r)$ analysis. $g(r)$ is computed in a 20-Å thick slab that encompasses the original interface and its evolution is shown in Figure 8. The results for the crystalline and amorphous phases are consistent with those reported in the literature [26, 32].

According to the Ni-Al phase diagram [33], the dissolution of Ni in the Al half-crystal at 800 K draws a trajectory in the temperature-concentration space that traverses different Al-rich phases of the alloy system until reaching the equiatomic stoichiometry. These include $NiAl_3$ as well as Ni_2Al_3. At the same time, there is experimental evidence that melting occurs during reaction of Ni and Al in environments with atomic ratios close to 1:3 [34, 35]. Crystalline NiAl phases subsequently emerge from the melt, giving rise to a stable alloy. As it will be discussed in Section 4, simulations in the NpT ensemble prevent melting by thermostatting the exothermic release due to the Ni-Al reaction (≈0.32 eV per atom)‖. Simulations in the isobaric-isoenthalpic ensemble NpH, which preserve the enthalpy of the reaction and thus allow a free fluctuation of the temperature, will be discussed below.

The formation and growth of the amorphous phase continues up to a time of approximately 20 ns in our simulation. From there on, thermodynamics drives the system toward structures consistent with Fig. 5, *i.e.* B2 phases. Recrystallization of the amorphous phase into a B2 structure initiates at the interface, resulting in a metastable (nano) crystalline structure characterized by high-angle boundaries and uncorrelated grain orientations. Evidence for this nano crystalline B2 structure is provided in Figure 9, which shows a still frame of the final system 34 ns after equilibration taken 5 Å from the original interface location on the Al-rich side.

‖ This is obtained from Fig. 4 as $\Delta E_r = 0.5(E_{\rm Ni} + E_{\rm Al}) - E^{am}_{\rm NiAl}$, which, at 800 K, is $\Delta E_r \approx 0.5(-4.35 - 3.19) + 4.09 = -0.32$ eV per atom.

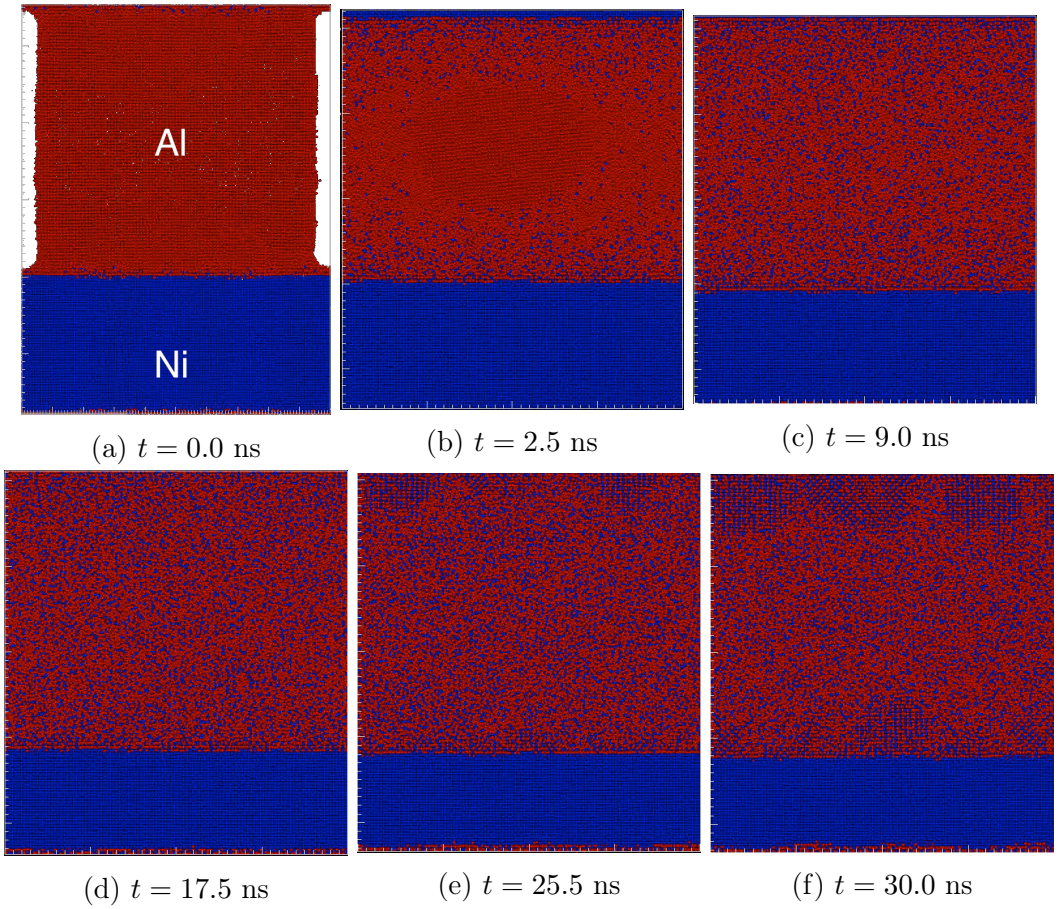

(a) $t = 0.0$ ns (b) $t = 2.5$ ns (c) $t = 9.0$ ns

(d) $t = 17.5$ ns (e) $t = 25.5$ ns (f) $t = 30.0$ ns

Figure 7: Time sequence of the reaction process in a Ni-Al bilayer at 800 K. Red circles represent Al atoms, blue circles symbolize Ni atoms. (a) Initial system during equilibration. (b) Beginning of the mixing process. Ni penetrates into Al much more than vice versa. (c) Mixing process is nearly complete, amorphization starts. (d) Mixing complete, all amorphous. (e) Crystallization in a B2 (bcc) phase starts at the interface. Crystallization starts where the local composition is close to equiatomic. (f) Crystallization proceeds.

The image shows atoms colored according to their Ackland-Jones parameter [36], which shows the formation of a nano grained bcc structure close to equiatomic composition¶. Therefore, the analysis is conclusive in terms of the final phase formed,

¶ According to the lammps convention, the Ackland-Jones parameter takes values of 0 (blue):

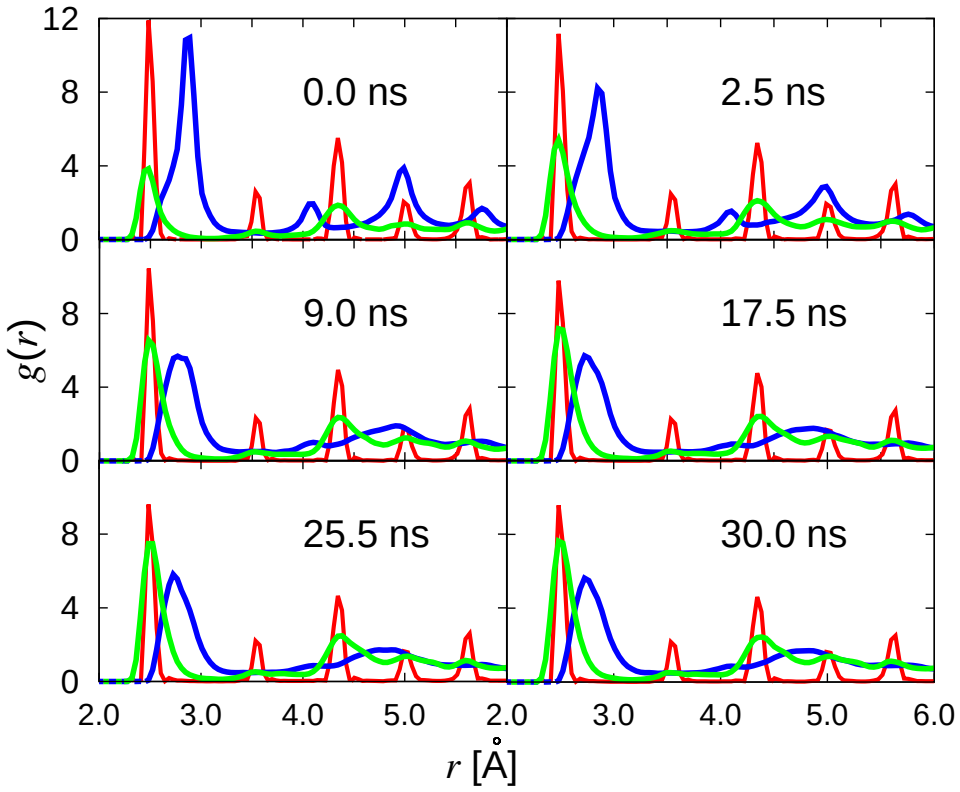

Figure 8: Evolution of $g(r)$ for Ni-Ni (red), Al-Al (blue), and Ni-Al (green) pairs for each of the snapshots shown in Fig. 7.

and is consistent with the free energy calculations observed in previous sections. It is expected that this B2 nano crystalline phase will coalesce over longer time scales and lead to a more stable coarsened structure.

unknown, 1 (cyan): bcc, 2 (green): fcc, 3 (yellow): hcp, and 4 (red): icosahedral.

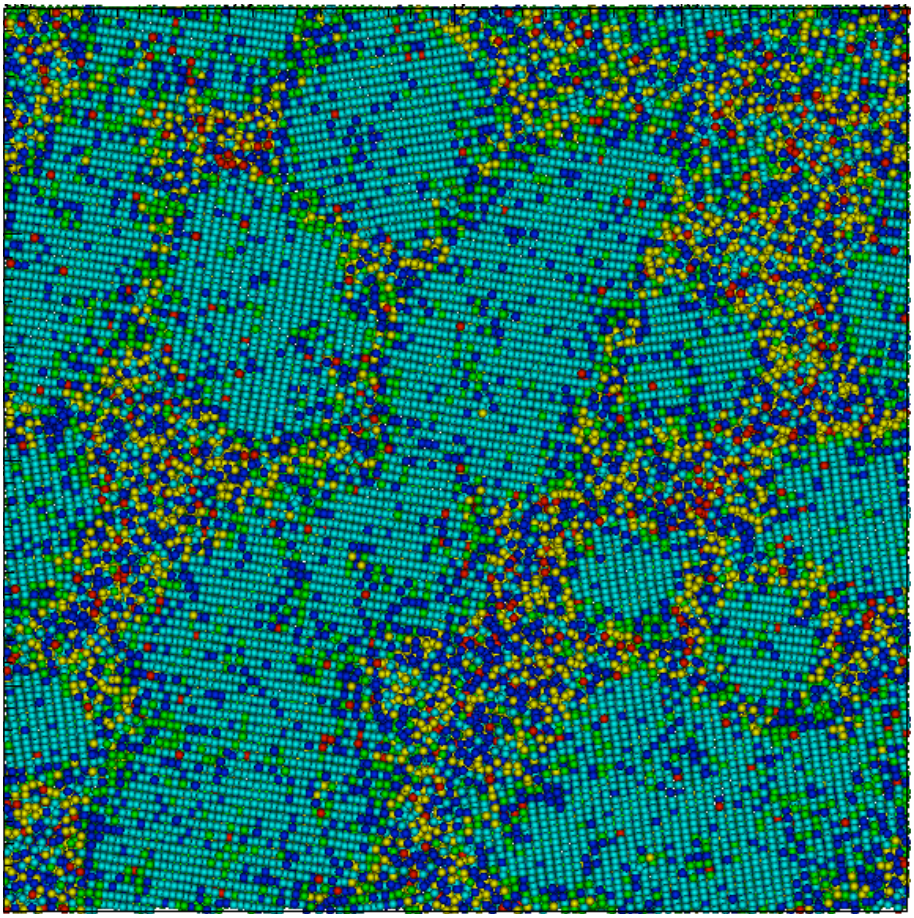

Figure 9: Crystal structure at the end of a 34-ns simulation of Ni-Al at 1000 K. The image corresponds to a cut parallel to the original Ni-Al interface taken at a distance of 5 Å into the Al layer. The observed microstructure consists of several B2 grains of approximately 5 nm in size. The structure was quenched from 800 K to remove thermal noise and make visualization clearer.

4. Discussion

4.1. Thermodynamics of Ni-Al compounds

Results in Table 1 match, where appropriate, those obtained by Purja and Mishin [17], and are in good agreement with those reported by Wang *et al* [27] at low

temperatures. However, our calculations do not include zero-point motion at low temperatures and are thus technically only suited for temperatures above the Debye temperature (≈430 and 450 K for Al and Ni, respectively). Therefore, comparison with low-temperature *ab initio* calculations should bear this fact in mind.

4.2. Ni-Al Reaction kinetics and thermodynamics

Ni-Al mixing processes have been studied in the literature using atomistic simulations [28–32]. In our context, the reaction process can be understood as following a rectilinear path along the 800-K isotherm on the two-dimensional $F(c,T)$ surface shown in Fig. 6. The reaction process occurs via the formation of a mixing zone of diffuse nature, characterized by the penetration of Ni in the Al layer, that grows as Ni diffuses and reaches concentrations capable of resulting in stable Ni-Al compounds. There is atomistic evidence that the minimum temperature for the process to occur in this fashion is of the order of 700 K [37].

Because Ni interpenetration in Al is much larger than vice versa, the bilayer reaction can be thought of as a process where Ni arrives in the Al crystal and gradually increases its relative concentration from zero to 0.5. Thermodynamically, this is illustrated again in Fig. 6 via the chemical potential $\mu = \partial F/\partial c$ (where c is the Ni concentration), which is negative for all values of T up to $c \approx 0.8$. This trajectory means that any incremental addition of Ni results in a decrease of F and is therefore thermodynamically favored. However, in going from low Ni concentrations to $c \approx 0.5$ along the 800-K isotherm (or, in fact, any other), one crosses a region of the free energy surface where the amorphous phase displays a lower free energy than the bcc phase (at 800 K, between $c \gtrsim 0.08$ and $c \lesssim 0.40$). This is essentially what happens between 9.0 and 25.0 ns after the reaction initiation. As the Ni concentration continues to increase, the system evolves toward a disordered bcc configuration until an equiatomic compound is formed. At that point, following Fig. 5, a lowest-free-energy B2 phase forms, signaling the cessation of the kinetics explored with MD. The constitution of the bcc and B2 phases takes place according to classical (heterogeneous) nucleation, with nuclei appearing at the interface, which by this time is quite diffuse. Thus, the free energy calculations are entirely consistent with the reaction processes studied here.

Another important aspect worth mentioning is the exothermic heat release due to the Ni-Al reaction. As mentioned in Section 3.3, the excess heat resulting from

the formation of amorphous NiAl relative to isolated Ni and Al is approximately 0.32 eV per atom. In the absence of any mechanical work performed on the system, this would result in a temperature increase of:

$$\Delta T \approx \Delta E_r / C_p$$

which, taking the values for the heat capacity from Table 1, would results in temperature increases on the order of 1230 K. This is in agreement with other MD simulations using the same interatomic potential [31]. As discussed in Section 3.3, this would suggest melting of all the phases involved, which would likely result in different reaction kinetics. However, we must bear in mind that the system suffers a marked volume reduction in going from pure Al to amorphous Ni-Al (cf. Table 1). This results in an effective compression of the Al crystal (e.g. Fig. 7a which reduces the amount of heat available for internal heating. This, together with the use of suitable thermostats in the MD simulations ensures isothermal dynamics. Figure 10 shows a three-dimensional representation of the temperature evolution with time across the atomistic system for the simulation at 800 K, where the original interface is located at $x = 0$. As the figure shows, the system preserves a constant temperature as a function of time. Simulations at 1000 K result in with faster kinetics but otherwise qualitatively equivalent conclusions. The potential employed here predicts melting temperatures of 1700 and 1040 K for pure fcc Ni and Al, respectively [17], and so simulations at either 800 and 1000 K are in the sub liquid thermodynamic regime.

As mentioned earlier, we also performed simulations at 800 K in the NpH ensemble using the same geometry as for the NpT case. These reveal a slightly different picture. In this case, the latent heat released into the system during mixing results in a progressive heating as the amorphous Ni-Al phase forms. We have measured the rate of heating at ≈5 K/ns. After amorphization (mixing) is complete after approximately 15 ns, the total temperature increased to 905 K, which represents a 13% increase with respect to the initial temperature, and still below the melting point of Al and Ni-Al for this potential.

5. Conclusions

We have obtained the thermodynamic properties of intensive thermodynamic variables for the N-Al system as a function of structure and composition. We have performed atomistic simulations of the Ni-Al system at high homologous

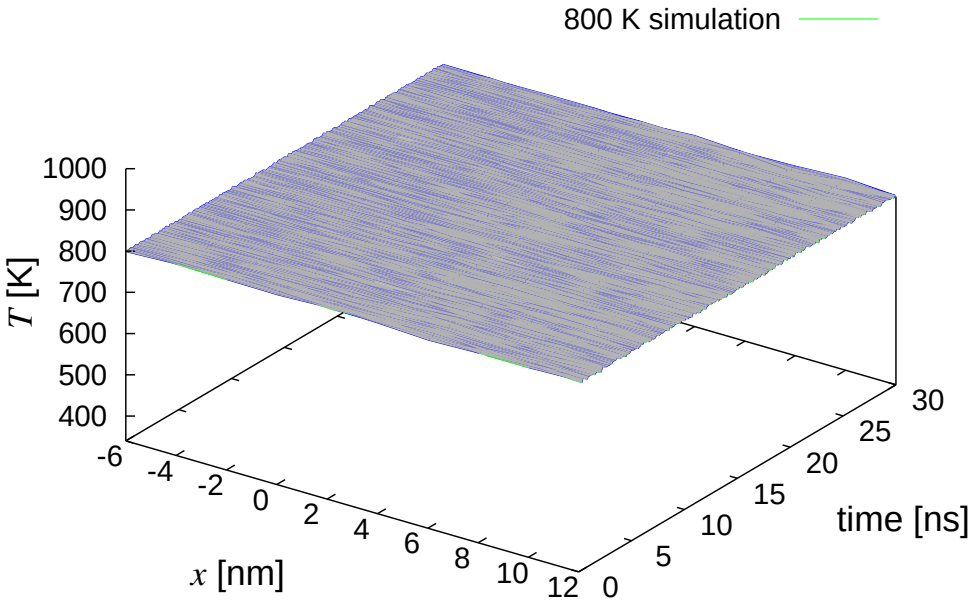

Figure 10: Time evolution of the temperature across the simulated bicrystal at 800 K. Each position represents a slab of material 2-nm thick over which the temperature is averaged. The original interface is located at $x = 0$. The temperature stays constant around 800 K.

temperatures and extracted several thermodynamic quantities for these conditions. This simulation methodology was then applied to a Ni-Al diffusion couple and its evolution observed. The Ni atom diffuses quickly into the Al and this alloying causes a structural transformation to an amorphous phase. In amorphous regions near the interface –where the composition first reaches the 1:1 ratio– nuclei of the B2 Ni-Al intermetallic phase form and grow. The absence of other intermetallic phases such as $NiAl_3$ or Ni_3Al may at first be counterintuitive because these compositions will at some point be present in the amorphous phase. However, the free energy calculations indicate that the B2 phase has a higher thermodynamic driving force for formation

that leads to more rapid kinetics. These other intermetallic phases are also not observed experimentally in systems with the small length scales and rapid kinetics considered here [6].

Acknowledgments

This work was performed under the auspices of the US Department of Energy by Lawrence Livermore National Laboratory under Contract DE-AC52-07NA27344.

References

[1] J. Duszczyk, J. Zhou, L. Marvina, L. Z. Zhuang, Journal of Materials Science **34** (1999) 3937.
[2] R. G. Nuzzo and L. H. Dubois, 'Intermetallic Compounds as Models for Materials Formed at the Metal Crystallite-Oxide Support Interface', in *Strong Metal-Support Interactions*, ACS Symposium Series, Vol. 298 (1986), Chapter 14, p. 136-144.
[3] A. S. Rogachev, Russian Chemical Reviews **77** (2008) 21.
[4] K. Barmak, C. Michaelsen, and G. Lucadamo, J. Mater. Res. **12** (1997) 133.
[5] I. E. Gunduz, K. Fadenberger, M. Kokonou, C. Rebholz, C. C. Doumanidis, and T. Ando, Journal of Applied Physics **105** (2009)
[6] J. S. Kim, T. LaGrange, B. W. Reed, M. L. Taheri, M. R. Armstrong, W. E. King, N. D. Browning, G. H. Campbell, Science **321** (2008) 1472.
[7] J. S. Kim, T. LaGrange, B. W. Reed, R. Knepper, T. P. Weihs, N. D. Browning, G. H. Campbell, Acta Materialia **59** (2011) 3571.
[8] J. C. Trenkle, L. J. Koerner, M. W. Tate, N. Walker, S. M. Gruner, T. P. Weihs, and T. C. Hufnagel, J. Appl. Phys. **107** (2010) 113511.
[9] P. Swaminathan, M. D. Grapes, K. Woll, S. C. Barron, D. A. LaVan, and T. P. Weihs, J. Appl. Phys. **113** (2013) 143509.
[10] M. Vohra, M. Grapes, P. Swaminathan, T. P. Weihs, and O. M. Knio, J. Appl. Phys. **110** (2011) 123521.
[11] M. Salloum, O. M. Knio, Combustion and Flame **157** (2010) 288; *Ibid* p. 436; *Ibid* p. 1154.
[12] P. Geysermans, D. Gorse and V. Pontikis, J. Chem. Phys. **113** (2000) 6382.
[13] Jianguo Yu, Susan B. Sinnott, and Simon R. Phillpot, Phys. Rev. B **75** (2007) 085311.
[14] F. Delogu, Nanotechnology **18** (2007) 065708.
[15] A. V. Evteev, E.V. Levchenko, F. A. Hagel, I. V. Belova and G. E. Murch, Intermetallics **19** (2011) 934.
[16] S. Plimpton, J. Comp. Phys. **117** (1995) 1.
[17] G. P. Purja Pun, Y. Mishin, Phil. Mag. **89** (2009) 3245.
[18] J. G. Kirkwood, J. Chem. Phys. **3** (1935) 300.
[19] J. M. Rickman, R. LeSar, Annu. Rev. Mater. Res. **32** (2002) 195.
[20] M. Müller, P. Erhart, K. Albe, J. Phys.: Condens. Matter **19** (2007) 326220.

[21] M. Tuckerman, “Statistical Mechanics and Molecular Simulations" (Oxford University Press, 2008).
[22] E. G. Noya, C. Rey, L. J. Gallego, Journal of Non-Crystalline Solids **298** (2002) 60.
[23] J. C. Crone, J. Knap, P. W. Chung, and B. M. Rice, App. Phys. Lett. **98** (2011) 141910.
[24] F. Baras and O. Politano, Phys. Rev. B **84** (2011) 024113.
[25] S. Shankar and L. L. Seigle, Metallurgical Transactions A **9** (1978) 1467.
[26] J. B. Zhu, S. Wang, M. H. Qiao, W. N. Wang, K. N. Fan, Journal of Non-Crystalline Solids **353** (2007) 2638.
[27] Y. Wang, Z.-K. Liu, L.-Q. Chen, Acta Materialia **52** (2004) 2665.
[28] B. J. Henz, T. Hawa, and M. Zachariah, Molecular Simulation **35** (2009) 804.
[29] N. S. Weingarten, W. D. Mattson, A. D. Yau, T. P. Weihs, and B. M. Rice, J. Appl. Phys. **107** (2010) 093517.
[30] M. J. Cherukara, K. Guda Vishnu, and A. Strachan, Physical Review B **86** (2012) 075470.
[31] K. Guda Vishnu, M. J. Cherukara, H. Kim, and A. Strachan, Physical Review B **85** (2012) 184206.
[32] S. Izvekov and B. M. Rice, J. Chem. Phys. **137** (2012) 094704.
[33] T. B. Massalski, H. Okamoto, P. R. Subramanian, L. Kacprzak (Eds.), “Binary Alloy Phase Diagrams”, AMS International, Materials Park, OH (1990), p. 183.
[34] E. Ma, C. V. Thompson, L. A. Clevenger, and K. N. Tu, Appl. Phys. Lett. **57** (1990) 1262.
[35] P. Zhu, J. C. M Li, C. T. Liu, Materials Science and Engineering A **329-331** (2002) 57.
[36] G. J. Ackland and A. P. Jones, Phys Rev B **73** (2006) 054104.
[37] C. Zhang, H. Wang, Y. Qiu, Engineering **3** (2011) 227.